LAWRENCE
LIVERMORE
NATIONAL
LABORATORY

LLNL-CONF-693612

Dynamic Compression Experiments

J. H. Eggert

June 1, 2016

High-pressure crystallography: status artis and emerging opportunities
Erice, Italy
May 28, 2016 through May 4, 2016

Disclaimer

Dynamic Compression Experiments

Jon Eggert, Lawrence Livermore National Laboratory

email: eggert1@llnl.gov

Abstract

Static and dynamic compression experiments are very different. In general, higher pressures can be obtained using dynamic compression, but with that come several advantages and disadvantages. Under dynamic compression, a time-dependent pressure drive is imposed on the material and the response of the material is measured. The compression is inertially confined and in a rigorous state of uniaxial strain. Many sources of entropy (manifested as increased temperature) are present, not all of which can be controlled. A variety of drivers can be used to generate dynamic compression and many specialized instruments are necessary to decipher the material states obtained. I will introduce some of the important concepts governing dynamic compression, the drivers employed, and the measurement techniques used.

Keywords

Dynamic, Shock, Ramp, VISAR, SOP

I. Dynamic Compression Fundamentals

Several overriding assumptions are often made extensively in understanding simple dynamic-compression experiments: 1) All material motion is one-dimensional, that is the experiment has planar, cylindrical, or spherical symmetry. This assumption (intertial confinement) simplifies the description significantly. 2) The conservation laws of mass, momentum, and energy for the system hold explicitly over the duration of the experiment. 3) The initial value condition of the pressure drive coupled with the conservation laws produce a set of hyperbolic differential equations that along with the constitutive properties of the material generates a systematic response of the system. 4) The material remains in Local Thermal Equilibrium (LTE) at all times. It is the goal of the experimentalist is to make measurements of physical observables to determine the material state constitutive properties.

For general one-dimensional flow of a compressible inviscid fluid, the continuous, hydrodynamic equations of motion can be written in the form of three conservation laws for mass, momentum, and energy:[1]

$$\frac{\partial \rho}{\partial t} = -\frac{\partial}{\partial x}(\rho u)$$
$$\frac{\partial}{\partial t}(\rho u) = -\frac{\partial}{\partial x}\left(\rho u^2 + P\right) \qquad (1)$$
$$\frac{\partial E}{\partial t} = -\frac{\partial}{\partial x}(Eu + Pu)$$

ρ is the local material density, u is the particle (local material) velocity, P is the pressure, and E is the internal (local material) energy. These hydrodynamic governing equations form a set of hyperbolic partial differential equations have can be generalized for solids[2] and require knowledge of material constitutive properties such as a P, ρ, E equation of state (EOS) strength model and phase diagram, to truly describe the material response. It is the determination of these constitutive properties that is the goal of most dynamic compression experiments. Note that entropy and temperature do not appear in the governing equations because the flow is purely isentropic for inviscid continuous flow.

In dynamic compression discussions two coordinate systems are often employed, Eulerian (laboratory, *x-t*) and Lagrangian (material, *h-t*). To convert the Eulerian governing equations above into Lagrangian coordinates we let $\rho_0 dh = \rho dx$, where h is the spatial (material) Lagrangian coordinate.[1] The first two governing equations can be rewritten for small waves in the form of the wave equation, $\frac{\partial^2 \rho}{\partial t^2} - C_E \frac{\partial^2 \rho}{\partial x^2} = \frac{\partial^2 \rho}{\partial t^2} - C_L \frac{\partial^2 \rho}{\partial h^2} = 0$, where C_E and C_L, $C_E^2 = \frac{\rho_0^2}{\rho^2} C_L^2 = \left.\frac{\partial P}{\partial \rho}\right|_S$ are the isentropic Eulerian and Lagrangian sound speeds respectively.

It is very useful to visualize a Lagrangian *h-t* plane where material perturbations can be drawn as lines. If a sudden perturbation is initiated at (x_0, t_0), one wave will propagate to the left and one to the right at velocities $\pm C_L$ ($u \pm C_E$, in Eulerian space). These waves comprise forward and backward characteristic waves with Riemann invariants, $du \pm d\sigma = 0$ along $\frac{dh}{dt} = \pm C_L$,

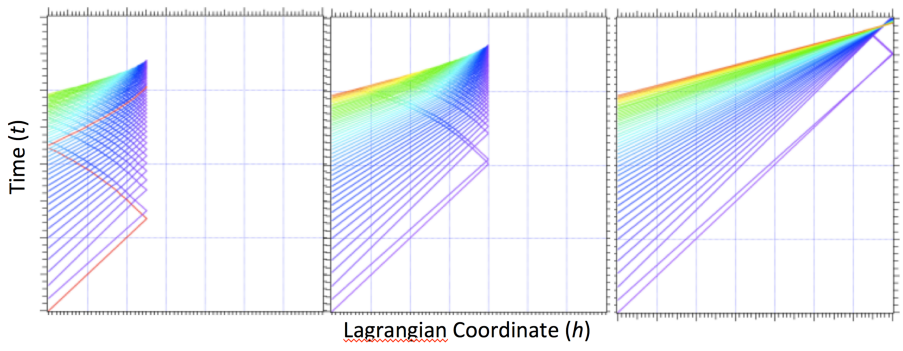

Fig. 1: Characteristics in Lagrangian coordinates plots showing dynamic compression of a nonlinear material with increasing sample thickness. For the thinnest sample, the free surface reverberation reaches the drive surface during the compression stage. For the intermediate sample the sample neither shocks before the free surface or reverberates to the drive surface. For the thickest sample a shock forms before breakout at the free surface. The fast initial wave in each sample represents the elastic response before plastic deformation where the characteristics travel at the faster elastic sound speed.

where $d\sigma = \frac{dP}{\rho_0 C_L} = \rho_0 C_L \frac{d\rho}{\rho^2}$.[1,3,11] J. R. Maw[12] has given a very nice, simple algorithm for propagating characteristics for simple ramp compressions waves used for the following figures.

Figure 1 shows a characteristics simulation in Lagrangian coordinates for three different sample thicknesses. Since materials generally display nonlinear compressibility so that the sound speed increases with pressure, the wave steepens as it transits the sample. Also shown in figure 1 are the characteristic response when the wave releases at the vacuum free surface. The interaction of the compression and release waves cause the characteristic lines to curve in space-time. Finally, the effect of elastic-plastic relaxation is shown by the drop in sound speed after the first two characteristics due to the drop in sound speed from the elastic to the bulk sound speed. Traditionally, dynamic compression experiments have relied on interface velocity measurements to determine the material constitutive properties. In figure 1 it is clear that ramp waves generally steepen into shocks after a sufficient time and thickness. If the drive reaches a final constant pressure, then a steady shock will form as the characteristics cross. The first governing equation can be integrated over a shock discontinuity occuring between x_1 and x_2,

$$\int_{x_0}^{x_1} \frac{\partial \rho}{\partial t} dx = -\int_{x_0}^{x_1} \frac{\partial}{\partial x}(\rho u) dx$$

$$\int_{x_0}^{x_s(t)} \frac{\partial \rho}{\partial x} dx + \int_{x_s(t)}^{x_1} \frac{\partial \rho}{\partial x} dx = u_0\rho_0 - u_1\rho_1$$

$$\rho_0 \frac{\partial x_s}{\partial t} - \rho_1 \frac{\partial x_s}{\partial t} + \int_{x_0}^{x_s(t)} \overline{\rho}\, dx + \int_{x_s(t)}^{x_1} \overline{\rho}\, dx = -\left(u_1\rho_1 - u_0\rho_0\right)$$

where ρ_0, u_0 and ρ_1, u_1 are the density and particle velocities immediately before and after the shock discontinuity. $D = \frac{\partial x_s}{\partial t}$ is the shock velocity and the integrals go to zero as $x_1 \to x_2$ so that, $\rho_0 D - \rho_1 D = -\left(u_1\rho_1 - u_0\rho_0\right)$, the mass conservation jump equation. Similar integrals can be done for the other governing equations giving the three Rankine-Hugoniot equations,

$$\begin{aligned} \rho_0\left(D - u_0\right) &= \rho\left(D - u\right) \\ P - P_0 &= \rho_0\left(D - u_0\right)\left(u - u_0\right) \\ E - E_0 &= \frac{1}{2}\left(P + P_0\right)\left(V_0 - V\right) \end{aligned} \qquad (2)$$

where $V = 1/\rho$. These three equations relate the thermodynamic state variables, ρ, P, E to the dynamic variables, *u* and *D* and the very specific locus of points accessible from an initial state, ρ_0, P_0, E_0 is called the Hugoniot. If two of these five variables are measured the other two can be calculated. Traditionally, the dynamic velocities *u* and *D* have been measured and the state variables calculated, but recently laser-driven dynamic compression experiments have allowed ρ to be measured directly by radiography, which combined with a single velocity measurement also closes the relations. It is often stated that the maximum compression from a strong shock is limited to $\rho/\rho_0 = 4$, this comes from the argument that after rewriting the energy equations as $E - E_0 = V/2\left(P + P_0\right)\left(\rho/\rho_0 - 1\right)$, substituting the ideal

gas EOS, $E = C_V PV$, and ignoring all terms containing P_0 as small compared to a strong shock pressure, one finds that $\rho/\rho_0 = 2C_V + 1$. Thus, the maximum compression for a monatomic ideal gas with $C_V = 3/2$ is four, while the maximum compression for a diatomic ideal gas is six.

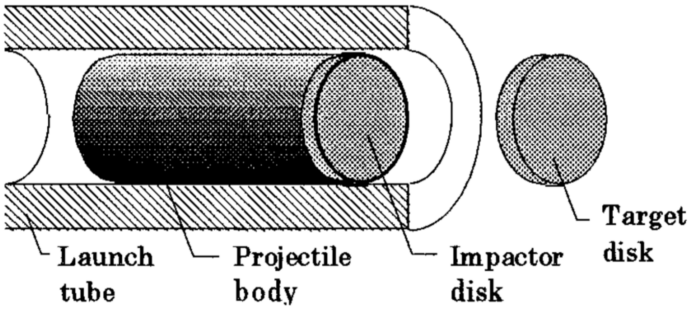

Fig. 2: (Taken from Davison's[2] Figure 3.2) "Schematic configuration of a plate-impact experiment. The projectile guides the impactor disk as it is accelerated along the launch tube (shown in cutaway view) by compressed gas or gun propellant. It collides with the target disk placed slightly beyond the end of the tube."

Absolute stress-density EOS measurement can be made using gas guns (figure 2) with a symmetric impact (same impactor and sample) as shown in figure 3. After a symmetric impact equal and opposite shocks propagate into both the impactor and the sample. In this case the experimental symmetry Rankine-Hugoniot relations both imply that the $u = u_{imp}/2$ where u_{imp} is the impactor velocity suggests that if both u_{imp} and the shock velocity, D, in either the impactor or the sample allow an absolute measurement of ρ, P, E on the sample Hugoniot. In the case of non-symmetric impact, ρ, P, E can still be determined, but the method involves impedance matching and requires a known standard.

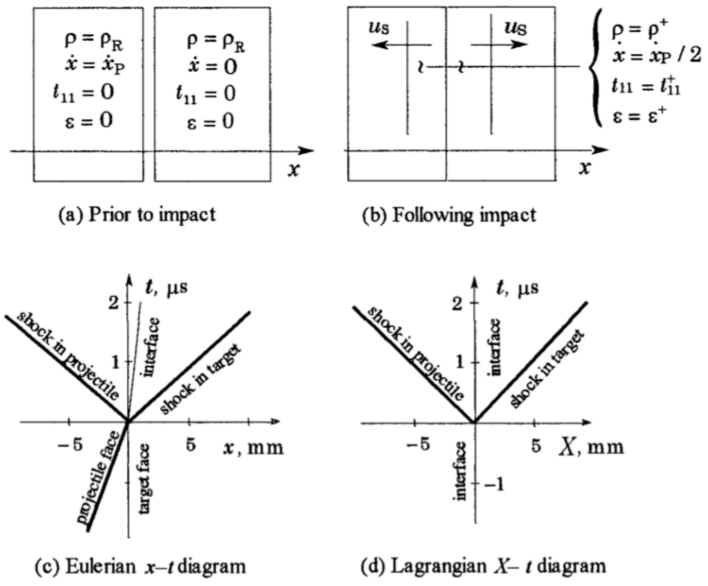

Fig. 3: (Taken from Davison's[2] Figure 3.3) "Plate-impact test configuration (side view) and space-time diagrams of the interaction. The side-view figures show the relative positions of the parts, indicate notation, etc., but the horizontal dimension is much too great in comparison to the vertical dimension for the figure to be scale representations of the actual parts."

While shock pressure and density can be measured absolutely by gas-gun symmetric impacts and by impedance matching, the temperature and entropy are much more difficult to constrain.

The continuous hydrodynamic equations for compressible inviscid flow (Eq. 1) are purely isentropic, but any irreversible constitutive response such as plastic relaxation or shock discontinuities will raise the entropy, and neither the temperature or the entropy are governed by conservation laws along the shock Hugoniot.[3] Since release from a shocked state is usually continuous, it is often true that shock release is isentropic.[4] In general (absent any constitutive information) the entropy rises as the third power of the shock strength, $z \equiv \left(P - P_0\right)/P_0$ (Whitham[3], ch. 6). While streaked optical pyrometry (SOP) can be used to determine the temperature in transparent samples that undergo a transition to a reflective state on the Hugoniot,[5-8] in general temperature is very difficult to measure. It has recently been shown that at special points on the Hugoniot the entropy can be determined by connecting the Hugoniot state to ambient pressure melting points,[9,10] but in general the shocked entropy is generally calculated quantity, and methods for measuring entropy and temperature remain an area of great necessity.

All high-pressure standards must be related to absolute stress-density standards like symmetric impact Hugoniot measurements.[13] But, as the shock strength increases into the multi-Mbar regime the shock temperature rapidly rises to several eV and all materials melt.[8] Thus, to provide pressure standards to static experiments and to study solid phases at very high pressures another method of compression is needed. Ramp compression can experiments fill both of these needs. As shown in figure 1 the hydrodynamic governing equations allow solutions of ramp compression steepening with time and sample thickness. If the pressure drive is carefully chosen then the inevitable shock in the material can be delayed until after the free-surface breakout. By comparing the free-surface velocity for various thickness samples the sound speed can be extracted and integrated to get absolute stress-density along relatively cold compression curves.[11,12,14,15] The ease of producing a shock-less drive improves for stiffer materials so that a large initial bulk modulus makes higher pressures possible. The two primary platforms for ramp compression EOS studies are lasers[11,16-19] and the Z-machine[15,20,21], although graded-density impactors are also used[22]. Materials with no or low strength can follow nearly isentropic compression curves and offer excellent potential to extend pressure calibration of standards to much higher pressures,[20] likely above 1 TPa in the near future[23]. Finally, modifications to the ramp-compressed sample configuration has allowed x-ray diffraction using laser-driven compression well into the TPa regime.[24-26] Of particular use for designing laser-driven compression experiments are several heuristic intensity versus pressure fits that allow pressure drives to be estimated without any need for complex or expensive simulation.[27-29]

II. Dynamic Compression VISAR Diagnostic

Dynamic compression diagnostics are many, but by far the most important diagnostic to this discussion is the VISAR (Velocity Interferometer System for Any Reflector),[30] and I will limit discussion of diagnostics to the VISAR. As the name implies, the VISAR is used to measure the velocity of interfaces by reflecting light from the interface. The line VISAR allows images the sample interface in one dimension (1-D) so that the drive planarity or multiple sample steps can be evaluated.[31] An implementation of the line VISAR commonly used is shown in Figure 4. Other useful implementations of the VISAR are the 0-D point VISAR[32,33], and the high-resolution 2-D VISAR[34-36].

I will cover the analysis for line VISAR here since it is the most widely used and valuable for laser-compression experiments. This analysis was developed by Peter Celliers and this discussion draws heavily on his publication[31] and notes.

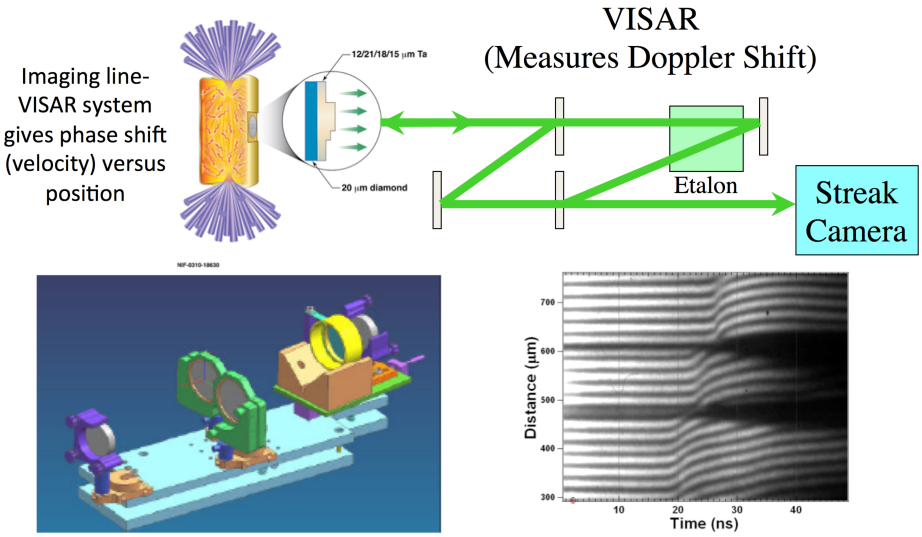

Fig. 4: The line VISAR diagnostic takes reflected laser light and runs it through a Mach-Zehnder interferometer. The spatial imaging properties of the line VISAR are essential to laser-driven compression experiments where shock planarity needs to be evaluated or where the velocity history varies with the sample position..

The line VISAR is a high resolution optical imager that projects a two-dimensional magnified image of the target onto a streak camera detector (Fig. 4). The reflected laser-light signal passes through a pair of velocity interferometers before being recorded on the streak cameras. The interferometers superimpose a sinusoidal spatial modulation on the image: Doppler shifts in the reflected probe are manifested as shifts of these fringes at the interferometer outputs. The streak cameras record the central slit region of the field of view and sweep this signal in time across the output detector. An optical delay is achieved by a combination of the refractive delay in the etalon and an additional translational offset of the etalon-mirror combination along a direction perpendicular to the mirror plane. The translation distance, $d = h\left(1 - 1/n\right)$, is calculated to place the image of the mirror plane as viewed through the etalon coincident with its initially determined null position (i.e., zero path delay with the etalon removed) . The resulting optical time delay is $\tau = \frac{2h}{c}\left(n - 1/n\right)$ where h is the etalon thickness, n is the index of refraction of the etalon, and c is the speed of light. The end mirror and the etalon in the delay arm of the interferometer are both mounted on a motorized translation stage.

When perfectly aligned (parallel output beams) , the Mach-Zehnder interferometer has a uniform output intensity: a single phase across the output. For the line-imaging application, a fringe comb is imposed on the output by slightly tilting the output beamsplitter, thus imposing a linear ramp in relative optical path difference across the output field. Doppler shifts in the light passing through the interferometer result in changes in the optical phase at the output, and these in turn appear as shifts in fringe position. The spatial frequency of this imposed pattern is arbitrary and is usually set to provide from 12 to 25 fringes across the output image (See figure 4).

Such a velocity interferometer measures the two-point time autocorrelation function of the input beam. The electric field vector of the undelayed path of the beam at the output of the interferometer is

$$\vec{E}(t) = E_0 \exp\left[-i\phi(t)\right] \tag{3}$$

where $\phi(t)$ is a phase function that contains terms accounting for the Doppler shift generated during the experiment. The phase function is given by,

$$\phi(t) = \int_{-\infty}^{t} \omega(t)dt + \phi_r(t) + \phi_p \tag{4}$$

The term $\phi_r(t)$ represents the optical phase shift upon reflection at the reflecting surface, and ϕ_p is a constant phase offset related to details of the fixed path in the interferometer, resulting for example from a slight tilt in the beam splitter to produce a spatially varying fringe comb at the output. The frequency of the reflected probe laser ω(t) contains a (non- relativistic) Doppler shift so that

$$\omega(t) = \omega_0 t \frac{1+u(t)/c}{1-u(t)/c} \approx \omega_0 t\left(1+2u(t)/c\right)$$

where $u(t)$ is the velocity of the free surface.

The interference pattern is produced when the illumination beam is split, and recombined with a copy of itself delayed by time τ, i.e. from the interference of the field $\vec{E}(t)$ with $\vec{E}(t+\tau)$. From Eq. 3 and Eq. 4 the interference term is,

$$2\left\langle \vec{E}(t) \bullet \vec{E}(t-\tau) \right\rangle = 2\left|E_0\right|^2 \exp\left(-i\left[(1+\delta)\int_{t-\tau}^{t} \Delta\omega(t)dt + \omega_0\tau + \phi_r(t) + \phi_r(t-\tau) + \phi_{p1} - \phi_{p2}\right]\right). \tag{5}$$

The argument of the exponential term represents the phase of the interferogram, and is time dependent through its dependence on $\Delta\omega(t)$ The total phase is the observable in the experiment,

$$\phi_V(t) = \frac{2\omega_0(1+\delta)}{c}\int_{t-\tau}^{t} \Delta\omega(t)dt + \omega_0\tau + \Delta\phi \tag{6}$$

where $\Delta\phi = \phi_r(t) + \phi_r(t-\tau) + \phi_{p1} - \phi_{p2}$ is constant over time scales $t > \tau$. Also introduced here is a correction factor $(1+\delta)$ which accounts for an additional phase shift that is caused by dispersion in the glass delay etalon. The dispersion in the delay etalon causes the Doppler shifted light to encounter a slightly different delay τ than unshifted light. While this slight change in the value of τ is negligible for experimental timing, it is significant compared to a single optical period, and thus is measureable with the interferometer, and results in an extra amount of observable phase relative to what one would observed with a dispersionless delay element (δ = 0.0315 at 532 nm in a fused silica etalon).

The integral in the first term of Eq. 6 can be interpreted formally as representing a moving average of the velocity over the etalon delay time τ, and centered at time $t - \tau/2$.

$$\phi_V(t) = \frac{2\omega_0\tau(1+\delta)}{c}\left\langle u\left(t-\tau/2\right)\right\rangle_\tau + \text{const} \tag{7}$$

or equivalently (dropping the constant phase offset),

$$\left\langle u(t)\right\rangle_\tau = \frac{\lambda}{2\tau(1+\delta)}\frac{\phi_V\left(t+\tau/2\right)}{2\pi} \tag{8}$$

the constant $\frac{\lambda}{2\tau(1+\delta)}$ defines the velocity per fringe (VPF) for the VISAR. This sensitivity

formula applies for Doppler shifts observed from free surfaces moving in vacuum. For many experiments this situation is not the case, and additional corrections must be factored in depending on details of the experiment. Hayes[37] has shown that for a complex windowed target system Eq. 8 is equivalent to $u_a(t) = dZ/dt$ where u_a is the apparent velocity denoted in Eq. 8 and Z is the total optical thickness between the reflecting surface and the interferometer beam splitter (in general, the only time-dependent path lengths are within the driven portion of the target). If the reflecting surface probed is a single reflecting shock, then the actual velocity, u_A, and the apparent velocity, u_a, are related by $u_A = u_a/n_0$, where n_0 is the refractive index of the initial state. Hayes[37] also showed that if the refractive index of a compressed window can be written as $n(\rho) = a + b\rho$ then $u_A = u_a/a$ independent of the time or position dependence of the compression wave. Since the refractive index of many sample windows can be fit relatively well to $n(\rho) = a + b\rho$ it is often assumed that the VISAR apparent velocity and the actual velocity are proportional to each other. In these special cases it is often assumed that $u_A(t) = VPF_A \frac{\phi_V(t+\tau/2)}{2\pi}$ where $VPF_A = \frac{\lambda}{2\tau(1+\delta)n^*}$ where n^* is n_0 for a reflecting shock, or a for a transparent window with an index defined by $n(\rho) = a + b\rho$. The relationship between the actual and apparent VISAR velocities enable several very clever methods of determining the refractive index of materials at high density and or temperature.[37-42]

Conclusions

I have tried to give a brief introduction to the basics of dynamic compression experiments, distinguishing shock and ramp compression experiments. Of particular importance to making quantitative measurements is the VISAR diagnostic and I have also introduced the basic concepts behind the diagnostic.

Acknowledgments

I thank all the members of the HED Shock Physics Group at LLNL who have taught me about dynamic compression physics, especially, Peter Celliers, Gilbert Collins, Dayne Fratanduono, and Yogi Gupta. This work was performed under the auspices of the U.S. Department of Energy by Lawrence Livermore National Laboratory under Contract DE-AC52-07NA27344. Lawrence Livermore National Security, LLC

References

1 Zel'dovich, Y. B. & Raizer, Y. P. *Physics of Shock Waves and High Temperature Hydrodynamic Phenomena*. (Academic Press, 1966).

2 Davison, L. *Fundamentals of Shock Wave Propagation in Solids*. (Springer-Verlag, 2008).

3 Whitham, G. B. *Linear and Nonlinear Waves*. (John Wiley & Sons, 1974).

4 Jeanloz, R. & Ahrens., T. J. Release Adiabat Measurements on Minerals: The Effect of Viscosity. *J. Geophys. Res.* **84**, 7545-7548 (1979).

5 Lyzenga, G. A. & Ahrens, T. J. Multiwavelength optical pyrometer for shock compression experiments. *Rev. Sci. Instrum.* **50**, 1421-1424 (1979).

6 Miller, J. E. *et al.* Streaked optical pyrometer system for laser-driven shock-wave experiments on OMEGA. *Rev. Sci. Instrum.* **78**, 034903 (2007).

7 Hicks, D. G. *et al.* Dissociation of Liquid Silica at High Pressures and Temperatures. *Phys. Rev. Lett.* **97**, 025502 (2006).

8 Eggert, J. H. *et al.* Melting temperature of diamond at ultrahigh pressure. *Nature Physics* **6**, 40-43 (2010).

9 Kraus, R. G. *et al.* Impact vaporization of planetesimal cores in the late stages of planet formation. *Nature Geoscience* **8**, 269-272 (2015).

10 Kraus, R. G. *et al.* Shock vaporization of silica and the thermodynamics of planetary impact events. *J. Geophys. Res.* **117**, E09009 (2012).

11 Fratanduono, D. E. *et al.* The effect of nearly steady shock waves in ramp compression experiments. *Journal of Applied Physics* **117**, 245903 (2015).

12 Maw, J. R. A characteristics code for analysis of isentropic compression experiments,. *AIP Conf. Proc.* **706**, 1217–1220 (2004).

13 Chijioke, A. D., Nellis, W. J., Soldatov, A. & Silvera, I. F. The ruby pressure standard to 150 GPa. *J. Appl. Phys.* **98**, 114905 (2005).

14 Rothman, S. D. & Maw, J. Characteristics analysis of Isentropic Compression Experiments (ICE). *J. Phys. IV France* **134**, 745 (2006).

15 Davis, J.-P., Brown, J. L., Knudson, M. D. & Lemke, R. W. Analysis of shockless dynamic compression data on solids to multi-megabar pressures: Application to tantalum. *J. Appl. Phys.* **116**, 204903 (2014).

16 Smith, R. F. *et al.* Stiff Response of Aluminum under Ultrafast Shockless Compression to 110 GPa. *Phys. Rev. Lett.* **98**, 065701 (2007).

17 Bradley, D. K. *et al.* Diamond at 800 GPa. *Phys. Rev. Lett.* **102**, 075503 (2009).

18 Smith, R. F. *et al.* Ramp compression of diamond to five terapascals. *Nature* **511**, 330-333 (2014).

19 Eggert, J. H. *et al.* Ramp compression of tantalum to 330 GPa. *High Pres. Res.* **35**, 339–354 (2015).

20 Kraus, R. G. *et al.* Dynamic compression of copper to over 450 GPa: A high-pressure standard. *Phys. Rev. B* **93**, 134105 (2016).

21 Eggert, J. *et al.* in *Shock Compression of Condensed Matter* (ed J. W. Forbes) 91 (AIP Press, 2007).

22 Yep, S. J., Belof, J. L., Orlikowski, D. A. & Nguyen, J. H. Fabrication and application of high impedance graded density impactors in light gas gun experiments. *Rev. Sci. Instrum.* **84**, 103909 (2013).

23 Fratanduono, D. Personal Communication. (2016).

24 Coppari, F. *et al.* Experimental evidence for a phase transition in magnesium oxide at exoplanet pressures. *Nature Geoscience* **6**, 926-929 (2013).

25 Lazicki, A. *et al.* X-Ray Diffraction of Solid Tin to 1.2 TPa. *Phys. Rev. Lett.* **115**, 075502 (2015).

26 Rygg, J. R. *et al.* Powder diffraction from solids in the terapascal regime. *Rev. Sci. Instrum.* **83**, 113904 (2012).

27 Fratanduono, D. E. *et al.* The direct measurement of ablation pressure driven by 351-nm laser radiation. *J. Appl. Phys.* **110**, 073110 (2011).

28 Swift, D. C. & Kraus, R. G. Properties of plastic ablators in laser-driven material dynamics experiments. *Phys. Rev. E* **77**, 066402 (2008).

29 Swift, D. C. *et al.* Shock formation and the ideal shape of ramp compression waves. *Phys. Rev. E* **115**, 066115 (2008).

30 Barker, L. M. & Hollenbach, R. E. Laser interferometer for measuring high velocities of any reflecting surface. *J. Appl. Phys.* **43**, 4669-4675 (1972).

31 Celliers, P. M. *et al.* Line-imaging velocimeter for shock diagnostics at the OMEGA laser facility *Rev. Sci. Instrum* **75**, 4916-4929 (2004).

32 Hemsing, W. F. Velocity sensing interferometer (VISAR) modification. *Rev. Sci. Instrum.* **50**, 73-78 (1979).

33 Dolan, D. H. Vol. SAND2006-1950 (ed Sandia National Laboratory) (Sandia Reports, 2006).

34 Erskine, D. J., Smith, R. F., Bolme, C. A., Celliers, P. M. & Collins, G. W. Two-dimensional imaging velocity interferometry: Data analysis techniques. *Rev. Sci. Instrum.* **83**, 043116 (2012).
35 Smith, R. F. *et al.* Heterogeneous flow and brittle failure in shock-compressed silicon. *J. Appl. Phys.* **114**, 133504 (2013).
36 Erskine, D. J. *et al.* Holographic and time-resolving ability of pulse-pair two-dimensional velocity interferometry. *Rev. Sci. Instrum.* **85**, 063115 (2014).
37 Hayes, D. Unsteady compression waves in interferometer windows. *J. Appl. Phys.* **89**, 6484-6486 (2001).
38 Fratanduono, D. E. *et al.* Refractive index of lithium fluoride ramp compressed to 800 GPa. *J. Appl. Phys.* **109**, 123521 (2011).
39 Fratanduono, D. E. *et al.* Index of refraction of shock-released materials. *J. Appl. Phys.* **110**, 083509 (2011).
40 Theobald, W. *et al.* X-ray preheating of window materials in direct-drive shock-wave timing experiments. *Phys. Plasmas* **13**, 122702(2006).
41 LaLone, B. M., Fat'yanov, O. V., Asay, J. R. & Gupta, Y. M. Velocity correction and refractive index changes for [100] lithium fluoride optical windows under shock compression, recompression, and unloading. *J. Appl. Phys.* **103**, 093505 (2008).
42 Setchell, R. E. Refractive index of sapphire at 532 nm under shock compression and release. *J. App. Phys.* **91**, 2833-2841 (2002).